# Characterisation of a Laser Plasma Betatron Source for High Resolution X-ray Imaging

**Contact:** oliver.finlay@cockcroft.ac.uk

**O.J. Finlay, M.J.V. Streeter, A.G.R. Thomas**[1]
*The Cockcroft Institute Daresbury Laboratory, Sci-Tech Daresbury, Daresbury, Warrington, WA4 4AD, United Kingdom*
*Lancaster University, Bailrigg, Lancaster LA1 4YW, United Kingdom*
[1] *also at Centre for Ultrafast Optical Science, University of Michigan, Ann Arbor, MI 48109 USA*

**D. Symes, R. Allott, C. Armstrong, N. Bourgeois, C. Brenner, C. Gregory, Y. Katzir, D. Neely, R. Pattathil, D. Rusby, C. Thornton**
*Central Laser Facility, Rutherford Appleton Laboratory, Didcot OX11 0QX, United Kingdom*

**S. Cipiccia**
*Diamond Light Source, STFC Rutherford Appleton Laboratory, Didcot OX11 0QX, United Kingdom*

**J.M. Cole, J. Gruse, N.C. Lopes**[2]**, S.P.D. Mangles, Z. Najmudin, J.C Wood**
*The John Adams Institute for Accelerator Science, Imperial College London, London SW7 2AZ, United Kingdom*
[2] *also at GoLP/Centro de Fisica dos Plasmas, Instituto Superior Tecnico, Lisboa, Portugal*

**C.D. Baird, C.D. Murphy, C. Underwood**
*York Plasma Institute, Department of Physics, University of York, York YO10 5DD, United Kingdom*

**L R Pickard**
*National Composites Centre, Bristol and Bath Science Park, Feynman Way Central, Emersons Green, Bristol BS16 7FS, UK*

**K D Potter**
*Advanced Composites Collaboration for Science and Innovation (ACCIS) University of Bristol, Bristol BS8 1TR, UK*

## Abstract

We report on the optimisation of an x-ray source, generated by a laser-driven plasma wakefield accelerator for an imaging experiment in Gemini Target Area 3. The highest x-ray signal was observed at a plasma electron density of $(4.4 \pm 0.2) \times 10^{18}\,\mathrm{cm}^{-3}$. This coincided with the highest observed electron beam charge measured by the electron spectrometer. The peak electron energy at this density was limited by dephasing to $0.52 \pm 0.12\,\mathrm{GeV}$. The spectra of the optimised source was consistent with an on-axis synchrotron spectra with a critical energy of $10.9^{+0.4}_{-0.3}\,\mathrm{keV}$ and the number of photons incident on the detector was calculated to be $(3.7 \pm 0.1) \times 10^{9}$. The x-ray beam was used to image a resolution grid placed 37 cm from the source, which gave an estimated spatial resolution of $4\,\mu\mathrm{m} \times 5\,\mu\mathrm{m}$. A number of samples were also imaged radiographically as part of ongoing work to develop laser plasma generated betatron radiation as a viable industrial imaging tool.

## 1 Introduction

Laser-driven plasma wakefield acceleration [1] is an established technique for the acceleration of electrons over very short distances [2, 3, 4]. The ponderomotive force of a short, intense laser pulse travelling though a plasma drives electrons away from regions of high intensity, creating a region of net positive charge. The electrostatic force then attracts the electrons back to their equilibrium positions and they begin to oscillate at a characteristic plasma frequency, $\omega_\mathrm{p} = (n_\mathrm{e} e^2/m_\mathrm{e}\epsilon_0)^{1/2}$ where $n_e$ is the plasma electron density. In the case of a strongly relativistic laser pulse, defined by a normalised vector potential $a_0 \gg 1$, almost all electrons are expelled by the pulse [5]. An approximately spherical ion cavity is formed in the wake of the laser which propagates at the reduced group velocity of the laser in the plasma, $v_\mathrm{g} = c(1 - (3/2)\omega_\mathrm{p}^2/\omega_\mathrm{L}^2)$ [6] where $\omega_\mathrm{L}$ is the angular frequency of the laser. The accelerating electric field in a laser wakefield accelerator (LWFA) can be estimated using the cold non-relativistic wave breaking field equation, $E_\mathrm{wb} = cm_\mathrm{e}\omega_\mathrm{p}/e$ [7]. From this it can be calculated that a density of $n_\mathrm{e} \sim 10^{18}\,\mathrm{cm}^{-3}$ can generate acceleration gradients around 100 GeV/m. The maximum energy gain of an electron in an electric field can be estimated as $W_\mathrm{max} = eEL_\mathrm{acc}$ where $L_\mathrm{acc}$ is the distance over which the electron feels the electric field. The challenge for LWFAs is increasing $L_\mathrm{acc}$, which for most current experiments is limited to a few millimetres. One major limitation to this is dephasing. Electrons can quickly be accelerated to a velocity of approximately c so can outrun the accelerating region of the wakefield [8]. In the 3D bubble regime for $a_0 >> 1$, the distance travelled by the electron in the time over which this dephasing takes place is given by:

$$L_\mathrm{d} = \frac{4}{3}\frac{\omega_\mathrm{L}^2}{\omega_\mathrm{p}^2}\frac{\sqrt{a_0}}{k_\mathrm{p}}\,, \tag{1}$$

where $k_\mathrm{p}$ is the plasma wave number. From this it can be seen that $L_\mathrm{d} \propto n_\mathrm{e}^{-3/2}$ [6].

Synchrotron-like radiation [9] is emitted in the electron direction of motion as accelerated electrons oscillate due to the focusing forces of the wakefield. The radiation source is defined by the betatron strength parameter, $\alpha_\beta$, which equals:

$$\alpha_\beta = r_\beta k_\mathrm{p} \gamma_\mathrm{e} \ , \tag{2}$$

where $r_\beta$ is the betatron amplitude and $\gamma_\mathrm{e}$ is the electron gamma factor [10]. The betatron parameter for a plasma source is equivalent to the deflection parameter, K, for conventional undulators/wigglers. Sources with $\alpha_\beta < 1$ are known as undulators and sources with $\alpha_\beta > 1$ are wigglers. The transverse electron motion in current LWFA experiments corresponds to $\alpha_\beta \sim 10$ [11] which is described by the wiggler regime. Assuming matched conditions and that the interaction length is equal to the dephasing length, the energy radiated by an electron bunch in an LWFA is:

$$E_\mathrm{rad} = \frac{\pi^{3/2}}{2} \gamma_\mathrm{p}^{7/2} a_0^5 m_e c^2 \ , \tag{3}$$

where $\gamma_\mathrm{p}$ is the associated Lorentz factor of the bubble [12]. From the group velocity of the laser in the plasma, for $\omega_\mathrm{L} \gg \omega_\mathrm{p}$ it can be shown that $\gamma_\mathrm{p} \propto n_e^{-1/2}$. The spectrum generated by the source is assumed to be an on-axis spectrum, so is defined only by the critical frequency, which is given by [13]:

$$\omega_\mathrm{c} = 3\alpha_\beta \gamma_\mathrm{e}^2 \omega_\beta \ , \tag{4}$$

where $\omega_\beta$ is the betatron frequency. The critical frequencies with current experimental parameters correspond to critical energies on the order of tens of keV. These x-rays can be used for both medical [14] and industrial [15] radiography to image micron-scale features in the internal structure of a material in a single shot of the drive laser. Radiation of this energy is more suited to radiography of relatively thin and/or low Z materials.

In this experiment, the generated X-ray signal from an LWFA was optimised through control of the plasma density in a single stage gas cell. The resolution of the optimised source was then characterised and applied to the imaging of industrial samples.

## 2 Experiment

The experiment was setup as shown in figure 1. The Gemini laser was focused using an f/40 off-axis parabola to a focal spot of FWHM size $50\,\mu$m $\times$ $40\,\mu$m at the entrance cone of the helium filled gas cell. The laser fully ionises the gas in its path and sets up a plasma oscillation in its wake. A pulse with a 45 fs FWHM with a central wavelength of 800 nm delivered $\sim 6$ J of energy on target giving a normalised vector potential $a_0 \approx 1.6$.

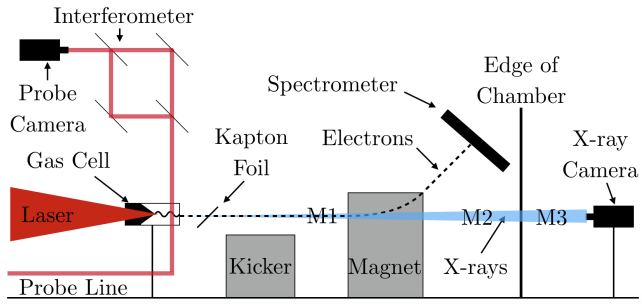


Figure 1: Simplified schematic of the experimental setup. The laser was focused at the gas cell entrance to drive the wake. The electron energy was calculated using the projection of the electrons onto a scintillating screen after being deflected by a magnetic field. An x-ray camera captured radiographic images of samples which could be imaged at either M1, M2 or M3 to give different geometric magnifications. The interferometric image from the probe camera was used to calculated the gas cell density. The kapton foil was used to reflect the drive laser light towards a beam dump and the kicker magnet could be used to deflect the electrons away from a sample if imaging at M1.

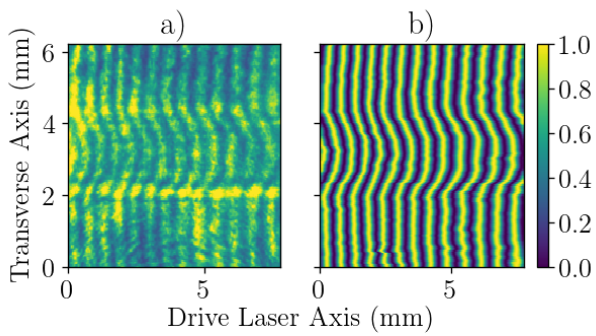


Figure 2: An interferogram - before, a), and after, b), filtering techniques had been applied - depicting the phase shift of the probe light as it travels through the plasma.

The gas cell length used for optimisation of the plasma wiggler source was 18 mm.

The electron spectrometer uses a Lanex scintillating screen to detect the accelerated electrons. A dipole magnet deflects electrons to different positions on the screen depending on their energy. The spectrometer was set up to detect electrons with energies between 100 MeV and 2 GeV. The x-ray camera used was an Andor iKon L 936 indirect detection camera [16] which consists of a CCD camera fibre-coupled to a structured $150\,\mu$m thick caesium iodide scintillator, allowing the detection of high energy photons. Objects to be imaged could be placed at one of three different positions - M1, M2 or M3 - along the beam line to give magnifications of 10, 2.5 or

1.6 respectively. The signal seen by the detector is given by:

$$\text{Counts} = \alpha N_\text{p} \int_0^\infty E\ S(E)\ Q(E)\ T(E)\ \text{d}E\ , \qquad (5)$$

where $\alpha$ is the counts per energy deposited calibration, $N_\text{p}$ is the number of photons incident on the scintillator and S is the synchrotron spectra of the source, which is dependent only on the critical energy of the source. Q is the quantum efficiency of the camera and T is the combined transmission function of the elements in the beam path. All of these parameters other than the number of photons and the critical energy of the synchrotron spectra are known. By normalising the signal to the signal with no added elements, the photon number can be ignored. The spectra emitted from the source can be found by imaging a number of thin slices of materials with known transmission functions. A one parameter minimisation of the measured signal over each material with respect to the theoretical signal can be used to find the critical energy of the emitted synchrotron spectrum. Once this is found, the number of photons incident on the scintillator can be calculated. Equation 5 also suggests two approaches to maximising the signal seen by the camera: increasing the number of photons and choosing an optimal source spectrum for the given imaging system.

The gas density, and therefore the plasma density, could be varied by changing the backing pressure of the gas injected into the cell. The plasma density for a given shot and a given backing pressure was measured from the phase shift seen by the probe interferometer. Leakage of the laser light was used to image the gas cell transversely after the plasma channel had been formed by the main beam. A Mach-Zehnder interferometer was used to interfere different parts of the same beam in order to distinguish the plasma channel. Since the refractive index of the plasma is lower than the surrounding neutral gas, a phase shift can be seen in the interferogram. An example raw interference pattern is shown in figure 2a. Due to intensity fluctuations of the incident probe beam, image filtering processes were needed to retrieve the phase. A Fourier filter was used in conjunction with a Hilbert transform based phase retrieval method [17][18] to extract the desired frequency components of the data. This resulted in a smooth interferogram with a clear phase pattern. An example of this is shown in figure 2b. Subtracting the constant phase leaves a phase shift given by [19]:

$$\Delta\phi(z,y) = \frac{2\pi}{\lambda_0} \int (\eta_\text{p}(x,y,z) - 1)\text{d}x\ , \qquad (6)$$

where $\eta_\text{p}$ is the plasma refractive index, $z$ is the laser axis, $x$ is in the axis of the probe light and the neutral gas refractive index is assumed to be one. From the dispersion relation of the light in the plasma $\eta_\text{p}$ can be written as $(1 - \omega_\text{p}^2/\omega_\text{L}^2)^{1/2}$. Assuming $\omega_\text{L} \gg \omega_\text{p}$, the phase shift can be written in terms of the line integrated plasma electron density:

$$\Delta\phi(z,y) = \frac{\lambda_0 e^2}{4\pi m_\text{e}\epsilon_0 c^2} \int n_\text{e}(x,y,z)\text{d}x\ . \qquad (7)$$

By rearranging this equation and assuming cylindrical symmetry, an Abel inversion can be applied to the phase shift to give a radial density profile,

$$n_\text{e}(z,r) = \frac{4 m_\text{e}\epsilon_0 c^2}{\lambda_0 e^2} \int_r^\infty \frac{\text{d}\Delta\phi}{\text{d}y} \frac{1}{\sqrt{y^2 - r^2}} \text{d}y\ . \qquad (8)$$

The plasma density was calculated by taking the average density along the central few pixels in the radial axis. This method was used to find a calibration between plasma density and gas backing pressure.

## 3 Results

### 3.1 Optimisation of the X-ray Source with Respect to Density

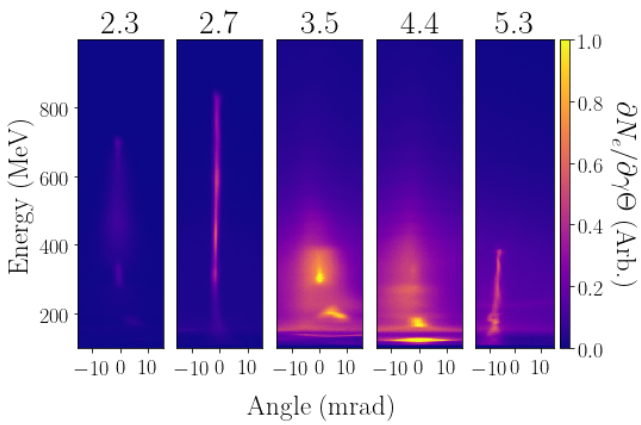


Figure 3: Angularly resolved electron spectra for different plasma densities. The plasma density given on top of each image is given in units $10^{18}\,\text{cm}^{-3}$.

Figure 3 shows how the angularly resolved electron spectra varies for different plasma densities. All of the images show beams with a small angular divergence, on the order of a couple of milliradians. For plasma electron densities of $3.5 \times 10^{18}\,\text{cm}^{-3}$ and $4.4 \times 10^{18}\,\text{cm}^{-3}$, the divergence of the electron beams seem to be much higher than at lower densities. It is thought that this is due, in part, to an interaction with the object being imaged, rather than it being a characteristic of the beams. The electron beam charge measured by the spectrometer and the maximum electron energy were averaged

over several shots, and plotted in figure 4. The maximum electron energy gain occurs at a plasma density of $2.7 \times 10^{18}\,\mathrm{cm}^{-3}$. As density increases, the dephasing length decreases as described earlier which limits energy gain. The highest electron bunch charge was seen at a plasma density of $(4.4 \pm 0.2) \times 10^{18}\,\mathrm{cm}^{-3}$.

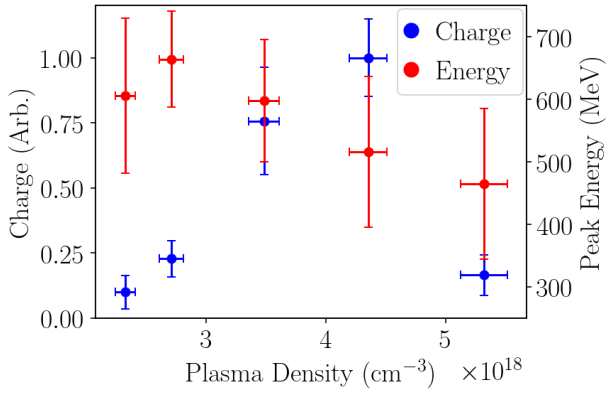


Figure 4: Plot showing the dependence of the electron bunch charge and maximum electron energy on the plasma density.

The integrated x-ray signal measured at different plasma densities is shown in figure 5. This signal is proportional to the energy deposited in the detector by x-ray photons. The signal scales in a similar manner with respect to the plasma density as the electron bunch charge, and the highest x-ray signal coincided with the plasma density at which the highest electron bunch charge was observed. The critical energy of the synchrotron spectrum emitted by the source at this density was $10.9^{+0.4}_{-0.3}$ keV. The quoted critical energy is the mean of critical energy found from ten filter array images with the same laser and plasma conditions. Using equation 5, the number of photons incident on the scintillator can also be calculated to be $(3.7 \pm 0.1) \times 10^{9}$. By maximising the integral term in equation 5, a critical energy of $E_c \approx 25$ keV can be calculated to be most efficient for this imaging system, giving approximately twice the signal seen at the measured critical energy for the same number of photons. This is a factor that should be considered in imaging experiments if the critical energy of the source can easily be modified.

### 3.2 X-ray Imaging with the Optimised Source

The resolution of this source was found by radiographically imaging a JIMA resolution grid [20], shown in figure 6. The smallest resolvable features horizontally are $\sim 4\,\mu$m, whilst the resolution limit vertically is $\sim 5\,\mu$m. The grid was 37 cm from the source and was imaged at a geometric magnification of $M \approx 10$. Line-outs of the

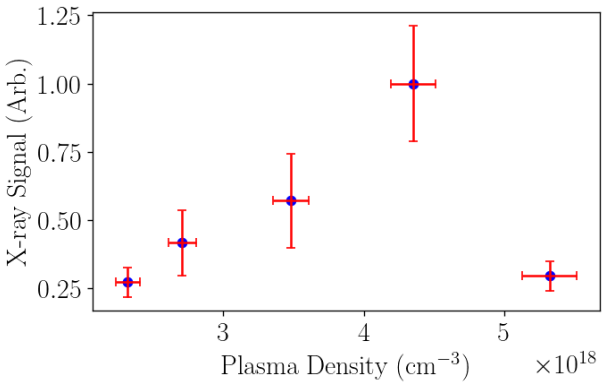


Figure 5: X-ray signal in arbitrary units for different plasma densities.

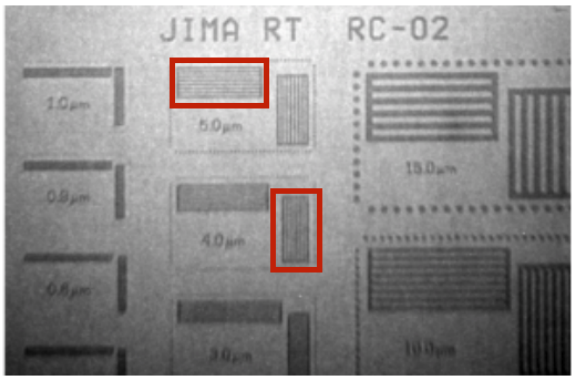


Figure 6: Radiographic image of a JIMA resolution grid. The red boxes highlight the smallest resolved features.

smallest resolved line-pairs and contrast transfer functions (CTFs) for both the horizontal and vertical line-pairs can be seen in figure 7. The CTF for the vertical line-pairs displays a sharp decrease in contrast for the smaller line-pair widths as would be expected. The horizontal CTF however is less well behaved. The contrast seems to not only depend on the line-pair width, but also the position of the line-pairs with respect to the centre of the beam. This is because the x-ray source has a finite length, which when imaging a sample off the beam axis at high magnification can be a limitation on the total image resolution. This effectively increases the transverse source size in the direction away from the beam centroid. The x-ray beam for this shot was centred above the resolution grid, which is why the effect of the longitudinal source size is so much more prevalent in the CTF of the horizontal line-pairs. Using the transmission of x-rays generated by this source, images were taken of a number of composite samples. Figure 8 shows two samples provided by the National Composite Centre [21] - a composite tee connection (7a) and a glass fibre disc in acrylic (7b) - imaged in this way. The materials imaged were

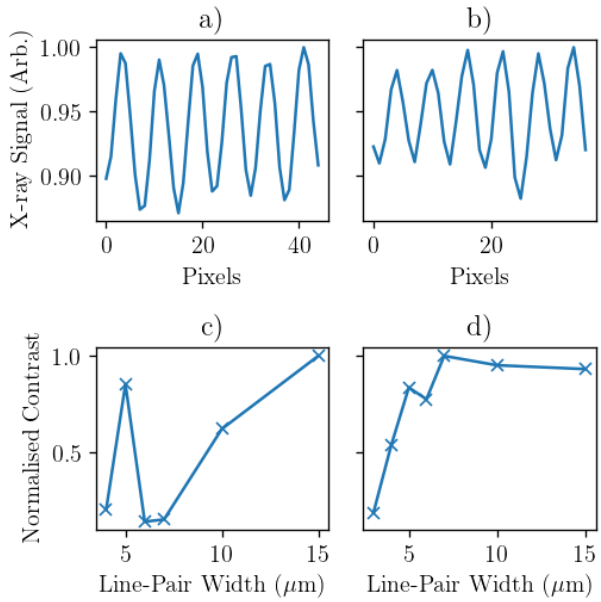


Figure 7: Line-outs for the minimum resolvable features for the horizontal, a), and vertical, b), grid lines are shown in the top two plots. The lower plots show the contrast measured for the horizontal, c), and vertical, d), line-pairs for different line-pair spacing.

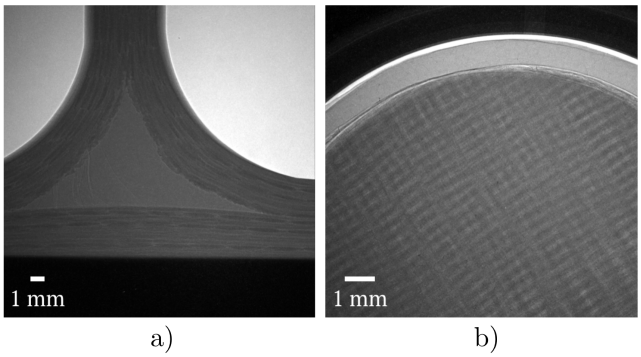


Figure 8: Composite samples imaged using the optimised plasma betatron x-ray source. a) is a composite tee connection, b) is a glass fibre disc in acrylic.

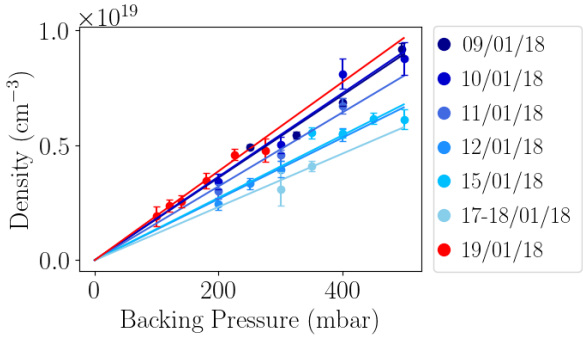


Figure 9: Backing pressure to plasma density calibrations at different points within the experiment. The key shows the date at which the calibration was measured. The gas cell exit cone was replaced before the calibration data was taken on 19/01/18.

| | Before Cell Change | After Cell Change |
|---|---|---|
| Density ($10^{18}$ cm$^{-3}$) | 3.47 ± 0.18 | 3.48 ± 0.13 |
| Average Max Electron Energy (MeV) | 599 ± 47 | 559 ± 118 |
| Average Electron Bunch Charge (Arb) | 0.36 ± 0.05 | 1.00 ± 0.30 |
| Average X-ray Signal (Arb) | 0.55 ± 0.02 | 1.00 ± 0.22 |

Table 1: Table showing the electron and x-ray properties for a similar plasma density before and after the gas cell exit cone was changed.

chosen based on their x-ray transmission properties. The x-ray penetration depth for the tee connection is $\sim 1$ cm which means some internal structure can be seen.

### 3.3 Effects of Gas Cell Damage

Throughout the experiment, the exit aperture to the cell sustained damage from the laser making it increase in size - from a few hundred $\mu$m to around 3 mm. As this aperture increased in size, a higher backing pressure had to be used to achieve the same plasma densities. The deterioration of the cell could be tracked by measuring the backing pressure needed to obtain a certain plasma density for the same laser conditions. Density to backing pressure calibrations throughout the experiment are shown in figure 9. It can be seen that the slope of the calibration line decreases throughout the experiment. This was attributed to the gas cell exit cone increasing in size, progressive damage by the drive laser. The gas cell exit cone was replaced with a new cone before shots were taken on 19/01/2018. The slope of the density calibration can be seen to increase again for this shot day. Note the density quoted here is the average density in the region transparent to the probe beam. This means features within the density profile in the laser axis which could be detrimental to the electron acceleration may be ob-

scured at the cell wall where the plasma density can not be measured. In order to determine if this is the case, electron beam and x-ray properties were compared at a similar measured plasma density, before and after the gas cell was changed. The results of this are shown in table 1. The maximum electron energy before the gas cell change was slightly higher, but the electron bunch charge and also x-ray signal are significantly larger after the exit cone was replaced. This could be due to a higher plasma density at the exit of the gas cell after the change in exit cone; promoting further injection. On the other hand, when the gas cell exit aperture is larger, there may be a lower plasma density at the cell exit due to outflow of the gas.

## 4 Conclusion

A compact x-ray imaging source capable of imaging centimetre scale composite structures has been demonstrated. Damage to the exit aperture of the gas cell was shown to be detrimental to the x-ray signal measured. It is essential that this is considered in the design of the gas cells when working with higher repetition rate lasers. A plasma density of $(4.4 \pm 0.2) \times 10^{18}\,\mathrm{cm}^{-3}$ was found to be optimal for imaging using a gas cell length of 18 mm. The spectra of this source was calculated to be on-axis synchrotron like with critical energy $10.9^{+0.4}_{-0.3}$ keV. An estimated resolution of $4\,\mu\mathrm{m} \times 5\,\mu\mathrm{m}$ was found at a high magnification. This is thought to have been limited by the length of the source, rather than the transverse size. Further experimentation on the tailoring of the longitudinal and transverse plasma density profiles in the gas cell can be performed in order to achieve lower resolution whilst maintaining the high x-ray signal. Expanding the number of optimisation parameters is crucial in order to obtain the best possible imaging source from LWFA and enabling industrial applications.

## Acknowledgements

The authors are very grateful for the hard work of the staff at the Central Laser Facility and for making this work possible. We acknowledge funding from STFC (grant numbers ST/P002056/1 and ST/P002021/1), and the EuroNNAc, Newton-Bhabha and Helmholtz ARD programs.

## References

[1] T. Tajima and J. M. Dawson. Laser Electron Accelerator. *Phys. Rev. Lett.* **43,** (4 1979), pp. 267–270.

[2] SPD Mangles et al. Monoenergetic beams of relativistic electrons from intense laser-plasma interactions. *nature* **431,** (2004), pp. 535–538.

[3] C. G. R. Geddes et al. High-quality electron beams from a laser wakefield accelerator using plasma-channel guiding. *Nature* **431,** (Sept. 2004), 538 EP –.

[4] J. Faure et al. A laser–plasma accelerator producing monoenergetic electron beams. *Nature* **431,** (Sept. 2004), 541 EP –.

[5] A. Pukhov and Meyer ter Vehn. Laser wake field acceleration: the highly non-linear broken-wave regime. *Applied Physics B* **74,** (4-5 2002), pp. 355–361.

[6] W. Lu et al. Generating multi-GeV electron bunches using single stage laser wakefield acceleration in a 3D nonlinear regime. *Phys. Rev. ST Accel. Beams* **10,** (6 2007), p. 061301.

[7] John M. Dawson. Nonlinear Electron Oscillations in a Cold Plasma. *Phys. Rev.* **113,** (2 1959), pp. 383–387.

[8] E. Esarey, C. B. Schroeder, and W. P. Leemans. Physics of laser-driven plasma-based electron accelerators. *Rev. Mod. Phys.* **81,** (3 2009), pp. 1229–1285.

[9] S Fourmaux et al. Demonstration of the synchrotron-type spectrum of laser-produced Betatron radiation. *New Journal of Physics* **13,** 3 (2011), p. 033017.

[10] E. Esarey et al. Synchrotron radiation from electron beams in plasma-focusing channels. *Phys. Rev. E* **65,** (2002), p. 056505.

[11] S. Corde et al. Femtosecond x rays from laser-plasma accelerators. *Rev. Mod. Phys.* **85,** (1 2013), pp. 1–48.

[12] A. G. R. Thomas. Scalings for radiation from plasma bubbles. *Physics of Plasmas* **17,** 5 (2010), p. 056708.

[13] John David Jackson. *Classical electrodynamics*. 3rd ed. New York, NY: Wiley, 1999.

[14] J M Cole et al. Tomography of human trabecular bone with a laser-wakefield driven x-ray source. *Plasma Physics and Controlled Fusion* **58,** 1 (2016), p. 014008.

[15] F. Albert and A.G.R. Thomas. Applications of laser wakefield accelerator-based light sources. *Plasma Physics and Controlled Fusion* **58,** 10 (Sept. 2016).

[16] Andor. URL: `http://www.andor.com/pdfs/specifications/Andor_iKon-L_936_Specifications.pdf`.

[17] Mitsuo Takeda, Hideki Ina, and Seiji Kobayashi. Fourier-transform method of fringe-pattern analysis for computer-based topography and interferometry. *J. Opt. Soc. Am.* **72,** 1 (1982), pp. 156–160.

[18] Violeta Madjarova, Hirofumi Kadono, and Satoru Toyooka. Dynamic speckle pattern interferometry (DESPI) phase analyses with temporal Hilbert transform. **11,** (Apr. 2003), pp. 617–23.

[19] I. H. Hutchinson. *Principles of Plasmsa Diagnostics*. Cambridge University Press, 2002.

[20] JIMA. URL: `http://www.jima.jp/content/pdf/catalog_rt_rc02b_eng.pdf`.

[21] National Composites Centre. URL: `https://nccuk.com`.